Height Determination of a Blue Discharge Observed by ASIM/MMIA on the International Space Station

Xue Bai, Martin Füllekrug, Olivier Chanrion, Serge Soula, Adam Peverell, Dakalo Mashao, Michael Kosch, Lasse Husbjerg, Nikolai Østgaard, Torsten Neubert, et al.

JGR Atmospheres

RESEARCH ARTICLE
10.1029/2022JD037460

Height Determination of a Blue Discharge Observed by ASIM/MMIA on the International Space Station

Xue Bai[1], Martin Füllekrug[1], Olivier Chanrion[2], Serge Soula[3], Adam Peverell[1], Dakalo Mashao[4,5], Michael Kosch[4,6,7], Lasse Husbjerg[2], Nikolai Østgaard[8], Torsten Neubert[2], and Victor Reglero[9]

[1]Centre for Space, Atmospheric and Oceanic Science, Department of Electronic and Electrical Engineering, University of Bath, Bath, UK, [2]National Space Institute, Technical University of Denmark, Copenhagen, Denmark, [3]Laboratoire d'Aérologie, Université de Toulouse, UT3, CNRS, IRD, Toulouse, France, [4]South African National Space Agency, Hermanus, South Africa, [5]Department of Physics, University of KwaZulu-Natal, Durban, South Africa, [6]Physics Department, Lancaster University, Lancaster, UK, [7]University of the Western Cape, Bellville, South Africa, [8]Department of Physics and Technology, Birkeland Centre for Space Science, University of Bergen, Bergen, Norway, [9]Image Processing Laboratory, University of Valencia, Valencia, Spain

Abstract We analyze simultaneous photometric observations of thundercloud discharges from the Modular Multispectral Imaging Array of the Atmosphere-Space Interactions Monitor (ASIM) on board the International Space Station with ground-based vertical electric field measurements in South Africa on 3 February 2019 at 23:00–23:05 UTC. During this time, ASIM flew over an extended thunderstorm front of several hundreds of kilometers and recorded a blue discharge with the photometer at 337 nm which emitted strong electric fields. It is found that the rising edge of the blue photomultiplier tube light pulse allows the estimation of the blue discharge height: ∼10.9–16.5 km which is constrained by cloud top height in a range of ∼13.3–16.7 km deduced from infrared radiometry on board the geostationary Meteosat satellite. The electric field measurements are used to infer the height of the blue discharge to be ∼16.0–18.8 km by use of skywave arrival times. It is shown that the height determinations are consistent with each other within the measurement uncertainties and the possible presence of an overshooting cloud top is discussed. The height of blue discharges is important to better understand how they can affect the chemistry in the upper troposphere.

Plain Language Summary Recently, Transient Luminous Events (TLEs) and lightning activity from thunderstorm tops above thunderstorms have attracted great interest. The Atmosphere-Space Interactions Monitor (ASIM) and the Modular Multispectral Imaging Array (MMIA) are on board the International Space Station to record the lightning activity and TLEs in the UV band (180–230 nm) as well as the blue (337 nm) and the red (777.4 nm) emissions. In total, 188 MMIA triggers were recorded and more than 2,000 lightning strokes were reported by the lightning detection and location network during 23:00–23:05 UTC on 3 February 2019. We focus on a blue discharge event that happened at 23:02:41 UTC. The novelty of this work is that the height determination is carried out by using ground-based electric field measurements and space-based optical measurements from ASIM. This study can help to understand the chemistry effects at the tropopause level caused by such blue discharge events.

Key Points:

- A blue discharge was detected by the Atmosphere-Space Interactions Monitor during an overpass of thunderstorms in South Africa
- The blue discharge height is determined by modeling the light propagation through the thundercloud constrained by cloud top heights
- The height of the blue discharge is also determined with ground-based electric field measurements of skywaves

Supporting Information:

Supporting Information may be found in the online version of this article.

Correspondence to:

X. Bai,
x.bai@bath.ac.uk

Citation:

Bai, X., Füllekrug, M., Chanrion, O., Soula, S., Peverell, A., Mashao, D., et al. (2023). Height determination of a blue discharge observed by ASIM/MMIA on the International Space Station. *Journal of Geophysical Research: Atmospheres*, *128*, e2022JD037460. https://doi.org/10.1029/2022JD037460

Received 10 JUL 2022
Accepted 17 MAR 2023

1. Introduction

Optical observations of lightning discharges are often compared to their electromagnetic signatures at radio frequencies, which are either recorded on board satellites or on the ground (e.g., A. R. Jacobson & Light, 2012; Peterson et al., 2021; Smith et al., 2004; van der Velde et al., 2020; Zhang & Cummins, 2020). The main rationale for this comparison is that the optical and electromagnetic signatures are both ultimately generated by the lightning discharge current. Most recently, scientific interest has focused on blue discharge processes near the top of thunderclouds which are indicative of an interesting streamer to leader transition (e.g., Chanrion et al., 2017; Chou et al., 2018; Husbjerg et al., 2022; Kuo et al., 2015; Li et al., 2021; F. Liu, Zhu, et al., 2021; F. Liu et al., 2018; Neubert et al., 2021). The first study of blue luminous events observed by the Atmosphere-Space Interactions Monitor (ASIM) was reported by Soler et al. (2020). Seven positive and three negative narrow bipolar events (NBEs) were observed by the ground-based receivers that were associated with blue band emissions, that is, 337 nm (F. Liu, Lu, et al., 2021). One of the key challenges in this area is to simulate the propagation of the light

emitted from the discharge process near the top of thunderclouds to the spacecraft (e.g., Brunner & Bitzer, 2020; Goodman et al., 1988; Luque et al., 2020; Peterson, 2019; Thomson & Krider, 1982). The inversion of such optical simulations can potentially be used to determine the height of blue discharges for comparison with the height inferred from the corresponding electromagnetic waveforms, which is the main aim of this contribution.

Global observations of Transient Luminous Events (TLEs) and lightning discharges have been conducted before by the Global LIghtning and sprite MeasurementS (GLIMS) mission on the International Space Station (ISS; Sato et al., 2015) and the Imager of Sprites and Upper Atmospheric Lightning (ISUAL) payload on board the FORMOSAT-2 satellite (e.g., Adachi et al., 2016; Chen et al., 2008; Chern et al., 2003) amongst other astronaut-led observations of TLEs on the ISS (e.g., Blanc et al., 2004; Chanrion et al., 2017; Yair et al., 2013) and the Space Shuttle (e.g., Price et al., 2004; O. H. Vaughan et al., 1992; Yair et al., 2003, 2005).

The Earth's ground and ionosphere form a nature waveguide to guide the radio wave propagation. The wave that travels along the ground is called the ground wave, while the wave reflected back and forth between the Earth–ionosphere cavity is called the skywave. The electromagnetic waveforms of energetic intracloud (IC) discharges are affected by propagation effects and therefore can be significantly influenced by the ground wave, which can lead to an attenuated peak amplitude, delayed zero-crossing time, and changed pulse width (Li et al., 2020). The height determination based on the time delay between the ground wave and first skywave becomes less reliable when the distance increases because the ground wave becomes more attenuated (e.g., Shao & Jacobson, 2009; Zhou et al., 2021). Smith et al. (2004) used a spherical Earth model of skywave propagation, where the ionospheric reflection height during the nighttime is more stable compared to the daytime, which was reported to be ~86 km.

The analysis reported in this contribution uses a fortuitous overpass of the ASIM/Modular Multispectral Imaging Array (MMIA) payload on board the ISS over an extended stretch of multiple thunderstorms in South Africa. During a time interval of 5 min, the MMIA payload ~400 km above the ground was triggered 188 times by exceptionally strong optical pulses, while >2,000 lightning strokes in the north-eastern part of South Africa were reported by ground-based lightning detection networks. The electromagnetic waveforms of the lightning strokes were recorded by a vertical electric field antenna, remotely located at Carnarvon in north-western South Africa at distances ~700–1,200 km from the lightning strokes. The 337 nm photometer of MMIA recorded a total of 87 blue pulses as part of the 188 triggers. Eight of these blue pulses exhibit relatively fast rise times <10 μs and large peak intensities, suggesting that the corresponding lightning strokes occurred near the top of the thunderclouds. One of these eight blue optical pulses was also associated with particularly large vertical electric fields which indicates that a strong blue discharge event occurred. This blue discharge event is discussed in detail in this paper. In order to geolocate the blue discharge to the ground, we assume it originates from the cloud top and projects the pixel corresponding to a maximum intensity of the blue discharge in the 337 nm camera at an altitude assumed to be 16 km. Knowing the ISS position and altitude at the time of the detection, the pixel is projected to longitude and latitude of 27.97°E and 26.47°S. It is noted that the projection is done with a zenith angle of 16.85°; this means that 1 km uncertainty in the altitude assumption corresponds to only 0.3 km uncertainty on the ground which is well within the uncertainty of the Meteosat pixel size. The experiment and data used are described in Section 2, the meteorological situation and storm structure is analyzed in Section 3, the space-based optical observations and ground-based electric field measurements are described in Section 4, the height determination with the electromagnetic signatures is explained in Section 5, and the simulations of the light propagation through the thundercloud are described in Section 6.

2. Measurements

2.1. Meteorology Measurements

Cloud top temperatures (CTTs) are recorded from the thermal infrared (IR) band at ~11–13 μm of the Spinning Enhanced Visible and Infrared Imager (SEVIRI) on board the Meteosat Second Generation (MSG) satellite operated by the European Organization for the Exploitation of Meteorological Satellites (EUMETSAT). The radiometer SEVIRI scans the Earth disk within about 12 min, from east to west due to the satellite rotation and from south to north due to the rotation of a scan mirror (Aminou et al., 1997). It provides images in 12 spectral bands every 15 min. The spatial resolution for the thermal channel is 0.027°, which corresponds to 3 km at the subsatellite point and about 3.5 km at the latitudes of the study area. The study area is therefore scanned 4 times

in 1 hr, around 2, 17, 32, and 47 min of each hour. The accuracy of the CTT values depends on several parameters, such as the type of clouds, the time during the day, and the geographic location on the Earth. In the study by Taylor et al. (2017), that compared SEVIRI CTTs from the new CLoud property dAtAset using SEVIRI, Edition 2 (CLAAS-2) data set against Cloud-Aerosol Lidar with Orthogonal Polarization (CALIOP) data, the uncertainty in night conditions was fluctuant between ∼0°C and 5°C in South Africa (Taylor et al., 2017, Figure 6). Thus, we consider in the present study the impact of an uncertainty of 2.5°C on the height determination, which is the mean value from Taylor et al. (2017) for this area. In order to analyze the meteorological conditions in which the storms developed on 3 February 2019 in the study area, we use the hourly ERA5 reanalysis performed by the European Copernicus/European Centre for Medium range Weather Forecast (ECMWF) data center for most of the atmospheric parameters (Hersbach et al., 2020). We also use reanalysis from the National Centers for Environmental Prediction (NCEP) and the National Center for Atmospheric Research (NCAR), specifically for the tropopause temperature because it is directly provided. Thus, the analysis considers the Convective Available Potential Energy (CAPE), geopotential height, wind at 500 hPa level, and the tropopause temperature.

2.2. Radio Waves Measurements

The vertical electric field waveforms are recorded with a flat plate antenna located in Carnarvon, 30.97°S, 21.98°E, in the north-west of South Africa. While the flat plate antenna can in principle record electromagnetic waveforms from ∼4 Hz to ∼1 GHz, the data acquisition unit uses a sampling frequency of 1 MHz to record the vertical electric field in the frequency range from ∼4 Hz to ∼400 kHz with an amplitude resolution of ∼40 μV/m and a timing accuracy ∼20 ns determined by a GPS disciplined oscillator (Füllekrug, 2010). This low-frequency (LF) receiver is remotely located in a desert location near the Square Kilometer Array with a controlled radio environment. There are not many strong LF transmitters in South Africa such that the electromagnetic recordings have a relatively small anthropogenic noise level when compared to recordings in northern Europe and therefore do not require filtering. As a result, this location is ideal for recording lightning waveforms that exhibit a clear separation between the ground wave and consecutive skywaves which arise from ionospheric reflections along the propagation path. The Vaisala Global Lightning Detection Network (GLD360) provides lightning information, which includes the lightning type, that is, cloud to ground (CG) or IC discharges, occurrence time, location, and peak current. The reported CG stroke detection efficiency of the GLD360 is ∼40%–60% (e.g., Said & Murphy, 2016; Said et al., 2010). The CG flashes are reconstructed from CG strokes by using criteria of continuity for time interval and distance between successive strokes, here 0.5 s and 10 km, respectively. Thus, for CG flashes, the detection efficiency is better than for CG strokes. The GLD360 data are mainly used for the meteorology study in Section 3. The occurrence time, location, and peak current of this blue discharge event are provided by Earth Networks Total Lightning Network (ENTLN; Marchand et al., 2019). A study evaluating ENTLN performance was carried out in Florida, which shows that the flash detection efficiency is 99% for natural lightning. The median location error and median peak current estimation error for rocket-triggered lightning are 215 m and 15% (Zhu et al., 2022). ENTLN is selected for providing the lightning information for this blue discharge event because its peak current estimation agrees more with our simulation results. More details are in Section 3.

South African Lightning Detection Network (SALDN) consists of 23 Vaisala lightning detection sensors, which detect the lightning electromagnetic signals by using the Time of Arrival and Magnetic Direction Finding techniques. The SALDN provides CG lightning stroke information, such as polarity, peak current, location, and occurrence time. The SALDN has an estimated 90% detection efficiency and ∼0.5 km location accuracy (Gijben, 2012).

2.3. Optical Measurements

The installation of ASIM with its MMIA on the ISS has recently significantly renewed interest to study lightning discharges, TLEs, and Terrestrial Gamma Ray Flashes from Low-Earth Orbit in near-Earth space (e.g., Chanrion et al., 2019; Neubert et al., 2019, 2020, 2021; Østgaard et al., 2021). The payload includes three photometers sampling light at 100 kHz in the following bands: 180–230 nm, 337 nm with a bandwidth of 4 nm, and 777.4 nm with a bandwidth of 5 nm. We will refer to them as UV, blue, and red, respectively, in the remainder of this contribution. Two cameras imaging in 337 nm with a bandwidth of 5 nm, and 777.4 nm with a bandwidth of 3 nm, at up to 12 frames per second, with a time resolution of 100 kHz, are also included in MMIA (Chanrion et al., 2019).

The typical location uncertainty of ASIM data is assumed to be 5 km. All MMIA instruments pointed toward the Nadir at the time of our observations.

3. Analysis of the Meteorology and Storm Structure

Figure 1b shows the geopotential height and the wind at 500 hPa, that is, the altitude of this pressure, with a colored scale in km and arrows, respectively. Low values of the geopotential form a trough in the southern part of the African continent between about 40°S and 30°S, insofar as they advance in an area of larger values. Thus, the low pressure area drives a clockwise flow around it, as it is indicated by the wind arrows. This flow is south-westerly in the western side of South Africa and westerly at about 20 m s^{-1} in the frame of the study which is crossed by the ISS path (Figure 1b). It can carry humid and warm air from over sea at this latitude. The map of CAPE in the area of the white frame in Figures 1a and 1b where storm activity was observed (Figure 1c) shows instability with large regions exhibiting values greater than 1 kJ kg^{-1} and locally values up to ∼2 kJ kg^{-1}. This distribution of CAPE can allow storms to develop for long periods and in a large area. Figure 1d shows the CG flash density for the period 14:00–02:00 UTC on 3–4 February, calculated with a resolution of 0.05° × 0.05°. This lightning density shows elongated southwest-northeast shapes that indicate the movement of thunderstorms in this direction, confirming the airflow generated by the pressure distribution (Figure 1b). The lightning flash density exceeds five flashes km^{-2} in some locations, which is very large for this 12-hr period. Figure 1e displays the CTT over the whole area of the frame (same as panels c and d) at 23:02 UTC, which is very close to the time of the blue discharge observation (23:02:41 UTC). It indicates the elongated structure of the storm activity including several cells with cold CTT (<−60°C) and convective cores with CTT < −70°C for some cells, especially the cell which produced the blue discharge at 23:02:41 UTC (indicated by a white cross in Figure 1e). At that time, the CTT of this cell has its coldest value (−74°C), but it corresponds to only one pixel (3.5 × 3.5 km^2). Since there is only one pixel with a temperature colder than the tropopause (−72.5°C according to Figure 1a), the cloud overshoot has a small horizontal extension. Thus, the resolution of the radiometer SEVIRI does not allow to determine the minimum of the CTT in such conditions with a large horizontal gradient as indicated in Figure 1f. Thus, the coldest temperature is probably smoothed and consequently the cloud height can be underestimated.

We can estimate the altitude of the cloud top from the ERA5 reanalyses provided by the ECMWF. These data provide the altitude and the temperature at different levels of pressure in the atmosphere. Figure 2 displays both altitude (blue curve) and temperature (orange curve) relative to pressure at the location of the cell producing the blue discharge. The minimum temperature observed for the atmosphere at 23:00 UTC (−72.5°C), which is therefore the tropopause, corresponds to a pressure of 100 hPa. This pressure corresponds to an altitude of 16.3 km, which is indicated by the black lines in Figure 2. Since the cloud top has a minimum temperature of −74°C (Figures 1e and 1f), it is 1.5°C less than the tropopause, which makes it 150 m above the tropopause according to the gradient of the adiabatic (−9.8°C/km) that can be used at this altitude where the air lifted by convection is dry (M. Jacobson, 2005). It is a small overshoot but it is consistent with low values of CAPE at this location (∼600 J kg^{-1}). The altitude of the cloud top is therefore near ∼16.4 km. If we take into account the location of the blue discharge from ASIM optical detection (white cross in Figure 1f), which is very close to the top of the cell, the temperature of the cloud top there is ∼−70°C. This temperature on the graph of Figure 2 corresponds to an altitude of ∼15.0 km (red lines projection). If we consider a circle of 5 km in radius around the blue discharge for the location uncertainty by ASIM, this leads to a range of temperatures in the interval (−74°C, −66°C). Furthermore, considering an error of ±2.5°C for the CTT, the corresponding new range of temperatures (−76.5°C, −63.5°C) corresponds to a maximum height of 16.7 km (0.4 km above the tropopause) and a minimum of 13.3 km (red dashed lines in Figure 2). However, if the real CTT values are colder than those determined at the resolution of 3.5 km × 3.5 km, these altitudes could be higher.

Figure 3 displays the rate of CG flashes detected within the cell that produced the blue discharge during 2 hr in panel (a) and the peak current of the CG strokes during 5 min (23:00–23:05 UTC) of the cell activity in panel (b). From (a), it seems the blue discharge occurs during a period with a relatively low CG flash rate (9.8 CG flashes min^{-1}) compared to a few tens of minutes later (>40 flashes min^{-1} at 23:55 UTC). Panel (b) confirms the low CG flash rate during the 5-min period where the blue discharge (blue triangle) was detected. Most CG strokes (from GLD360) are negative and gathered (vertically lined up on the graph) within sequences which correspond to CG flashes, separated of a few seconds and sometimes a few tens of seconds. The blue discharge at 23:02:41 UTC corresponds to a detection by ENTLN (−18.9 kA) and is not associated with another CG detection within 2 s. According to the wave propagation model introduced by Kolmašová et al. (2016) and Kašpar et al. (2017), the experimental attenuation coefficient can be calculated by knowing the propagation distances, peak currents,

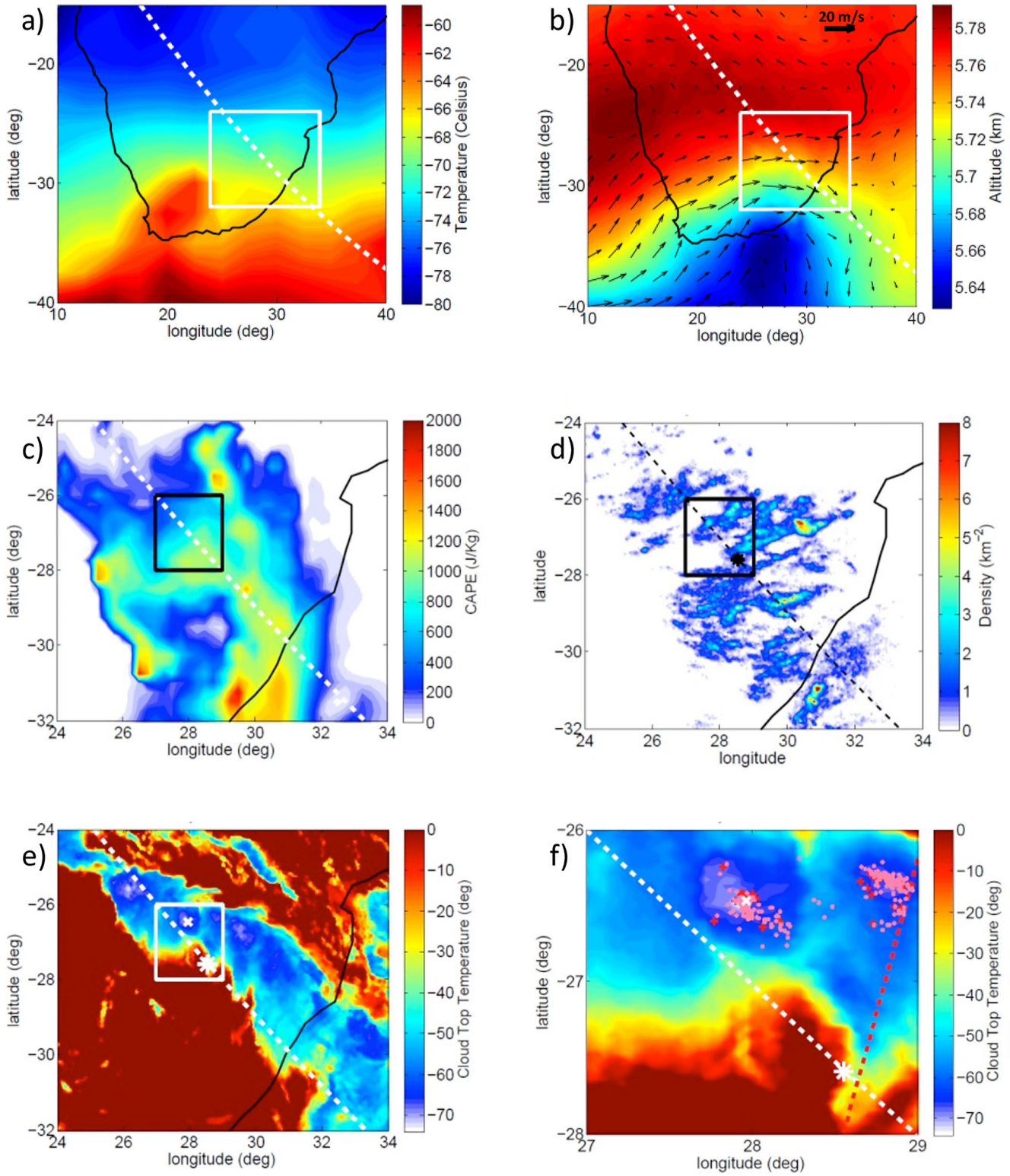

Figure 1.

and measured maximum electric fields of a group of lightning events (Bai & Füllekrug, 2022). In this work, the CG strokes recorded between 23:00:00 UTC and 23:00:05 UTC are used to estimate the experimental attenuation coefficient. Then, based on the propagation distance and the measured maximum electric field of this blue

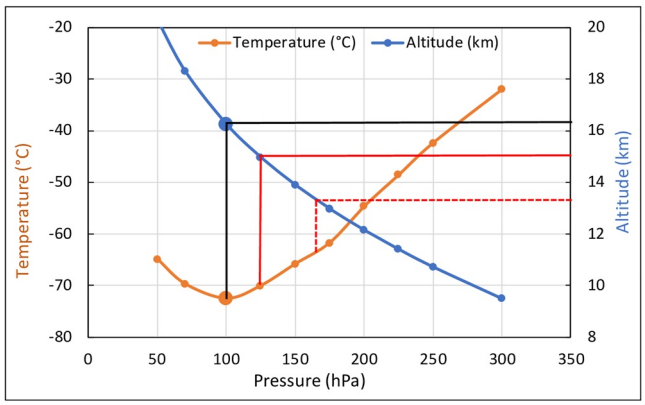

Figure 2. Temperature (orange curve) and altitude (blue curve) versus pressure, in the upper troposphere (8–20 km). The minimum of temperature is found at 100 hPa and corresponds with the tropopause at an altitude of 16.3 km (black lines). The red line indicates the cloud top temperature (CTT) observed at the location of the blue discharge (−70°C) and the correspondence with the altitude (15 km). The red dashed lines represent the uncertainty for the CTT derived from Spinning Enhanced Visible and Infrared Imager (SEVIRI; ±2.5°C) and from the location uncertainty of the blue discharge (5 km radius circle), which leads to a range of altitudes for the cloud top (13.3–16.7 km).

discharge event, the peak current is estimated to be −18.4 kA, which matches well with the peak current reported by ENTLN. The peak current reported by GLD360 for this blue discharge event is −11 kA. Therefore, the ENTLN is selected for providing the lightning information for this blue discharge event.

4. Space-Based Optical Measurements

The ISS with the ASIM/MMIA payload passes over South Africa, from 23:00 to 23:05 UTC on 3 February 2019 (Figure 1e). The track of the ISS crosses a front of thunderstorms which extends over several hundreds of kilometers and comprises numerous individual active cells. The crossing angle is relatively small such that the field of view of the MMIA photometers records optical pulses of lightning discharges for a relatively long duration of ∼5 min (Figure 1e).

The photomultiplier tube (PMT) traces for red (777.4 nm), blue (337 nm), and UV (180–230 nm) wavelengths exhibit large numbers of optical pulses above the background. The largest number of optical pulses is observed in the red PMT trace, followed by the blue and finally the UV trace which exhibits the smallest number of optical pulses. This general behavior is illustrated as an example in the lower three panels of Figure 4 and it is attributed to the wavelength-dependent scatter and absorption of the light propagating inside the thundercloud. The main aim of this contribution is to compare the optical emissions of lightning strokes to the corresponding vertical electric field recordings which are shown in the upper panel of Figure 4. The peaks of the envelope of the vertical electric field recordings are generally associated with the peaks of the optical pulses after referencing both records to known lightning flashes, as explained in more detail in the following paragraph. Some electric field pulses are not associated with optical pulses, for example, the electric field pulses at 33.52 and 33.66 s. These pulses might originate from lightning discharges outside the MMIA field of view, or the corresponding optical pulses from the lightning discharges are completely absorbed by the thundercloud.

The aim of this study is to investigate a blue discharge event near the top of a thundercloud. This event is therefore defined by two key criteria, namely that the event occurs near the cloud top, that is, <10 μs rise time of the optical waveform with large intensity, and that it is associated with a significant discharge process, that is, a relatively large vertical electric field intensity, as explained in the introduction. An exemplary blue PMT recording with a fast optical rise time, large optical intensity, and a strong electric field pulse is shown in Figure 5. The electric field recordings are referenced to the occurrence time (23:02:41.234970 UTC) and location (26.48°S, 27.95°E) of the blue discharge event as reported by ENTLN, after correction for the electromagnetic wave propagation time from the source location to the receiver at the speed of light. The observed electric field pulse is akin to a NBE which occurs near the top of the thundercloud such that several methods can be explored to determine the height of the event as described in the following section.

Although the image for this blue event was not downloaded to the ground, the camera metadata giving the sum of optical intensities along the rows and columns in the picture taken by the camera allows to find the geolocation of the peak intensity corresponding to the discharge with an uncertainty of ∼5 km.

5. Height Determination From Ground-Based Electric Field Measurements

The electric field recording of the blue discharge event is shown in Figure 6a. This is a negative lightning event recorded at 23:02:41.238 UTC on 3 February 2019. There are two pulses for both, the first and second skywave (Figures 5 and 6a), which indicates that the source height is high above ground. The complex analytic

Figure 1. Meteorological conditions on 3 February 2019. (a) Temperature of the tropopause in a large area including South Africa. (b) Geopotential (color) and wind (arrows) at the level 500 hPa in the same area at 18:00 UTC. The white frame indicates the area for (c)–(e) panels and the white dashed line the ISS path. (c) Convective Available Potential Energy (CAPE) values at 18:00 UTC in the area of the white frame. (d) Cloud to ground (CG) flash density from 14:00 on 3 February to 02:00 on 4 February, calculated at a resolution of 0.05° × 0.05° in the same area. (e) Cloud top temperature (CTT) in the same area at 23:02 UTC. (f) Zoom of the CTT on the thunder cell producing the blue discharge correspond to the squares shown in (c)–(e) at 23:02 UTC. The dashed line and the star indicate the path and the position at the detection time, of the International Space Station (ISS)/Atmosphere-Space Interactions Monitor (ASIM), respectively. The white cross in (e) and (f) indicates the location of the blue discharge by ASIM at 23:02:41 UTC. The red plus symbols and pink dots indicate the +CG and −CG flashes, respectively, detected by GLD between 23:00 and 23:05 UTC. The red dashed line is the CALIPSO track.

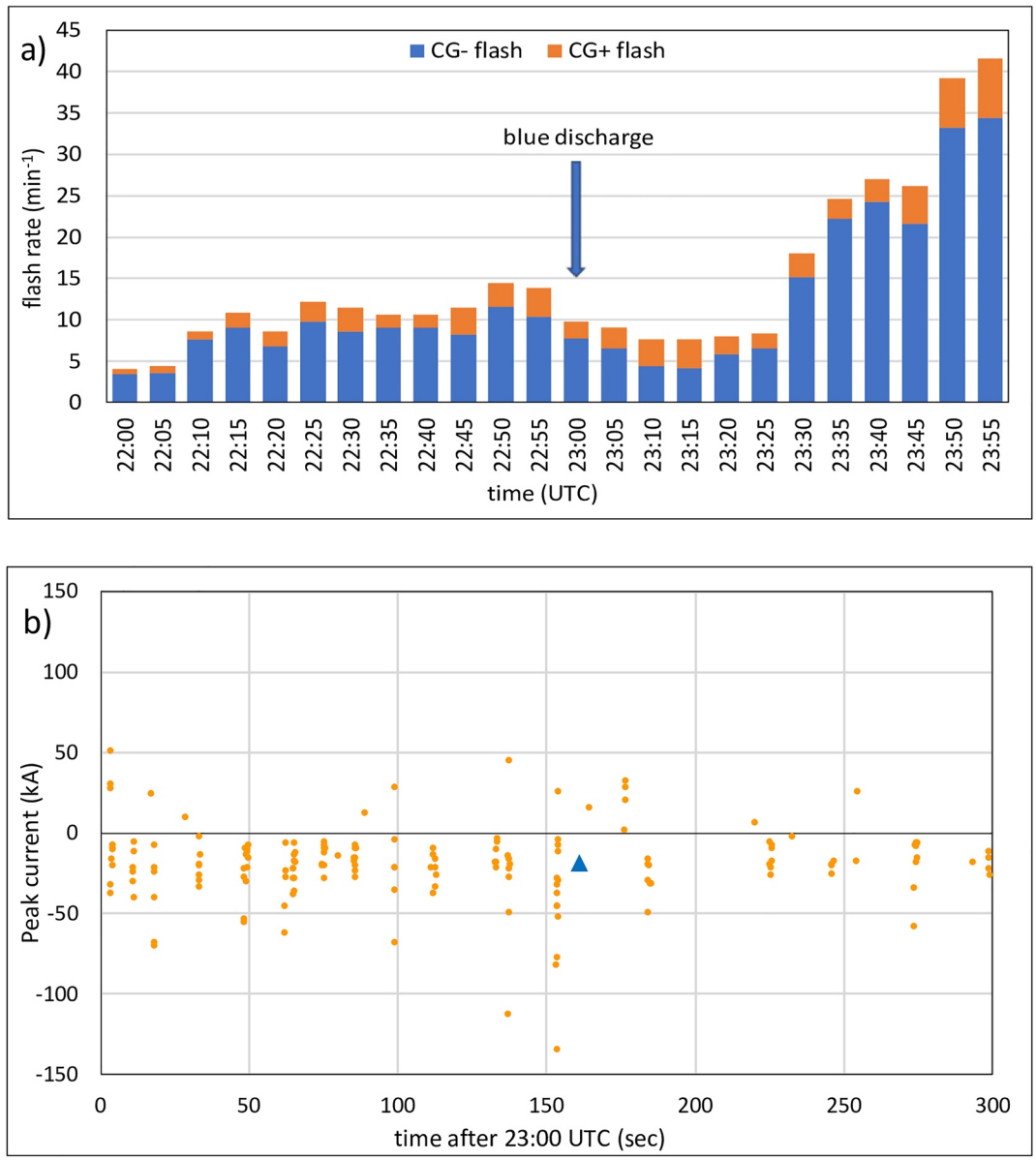

Figure 3. The cloud to ground (CG) lightning activity of the thunder cell producing the blue discharge (shown in panel f) of Figure 1: (a) CG flash rate during 2 hr from 22:00 UTC on 3 February to 00:00 UTC on 4 February; (b) peak current of CG strokes during 5 min from 23:00 UTC to 23:05 UTC on 3 February. The blue triangle in (b) indicates the detection by Earth Networks Total Lightning Network (ENTLN; −18.9 kA) at 23:02:41 UTC.

signal of this blue discharge event is calculated to help define the pulse peaks for both skywaves. The height determination is based on modeling the skywave propagation, and a simulation of the source height and the ionospheric reflection height. For long distance propagation, the ground wave is heavily attenuated during a long propagation path, and the rising edge of the ground wave is delayed during the propagation along the Earth's curvature (Hou et al., 2018). Therefore, the time delays between the two skywaves are used in this work. The time delays Δt_1 and Δt_2 are marked in Figure 6a. The time delay Δt_1 refers to the time delay of the ionospheric reflections of the first skywave and second skywave in the ionospheric reflection model in Figure 6b. The time delay Δt_2 is the time delay of the ground reflections of these two skywaves in the ground reflection model in Figure 6c. The absolute value of the analytic signal of this event is calculated to ensure that the two skywaves exhibit unique local maxima and to rule out the possibility of misidentification. The receiver used in this work was placed at an altitude of 1.341 km (Füllekrug et al., 2019) which is also considered in this

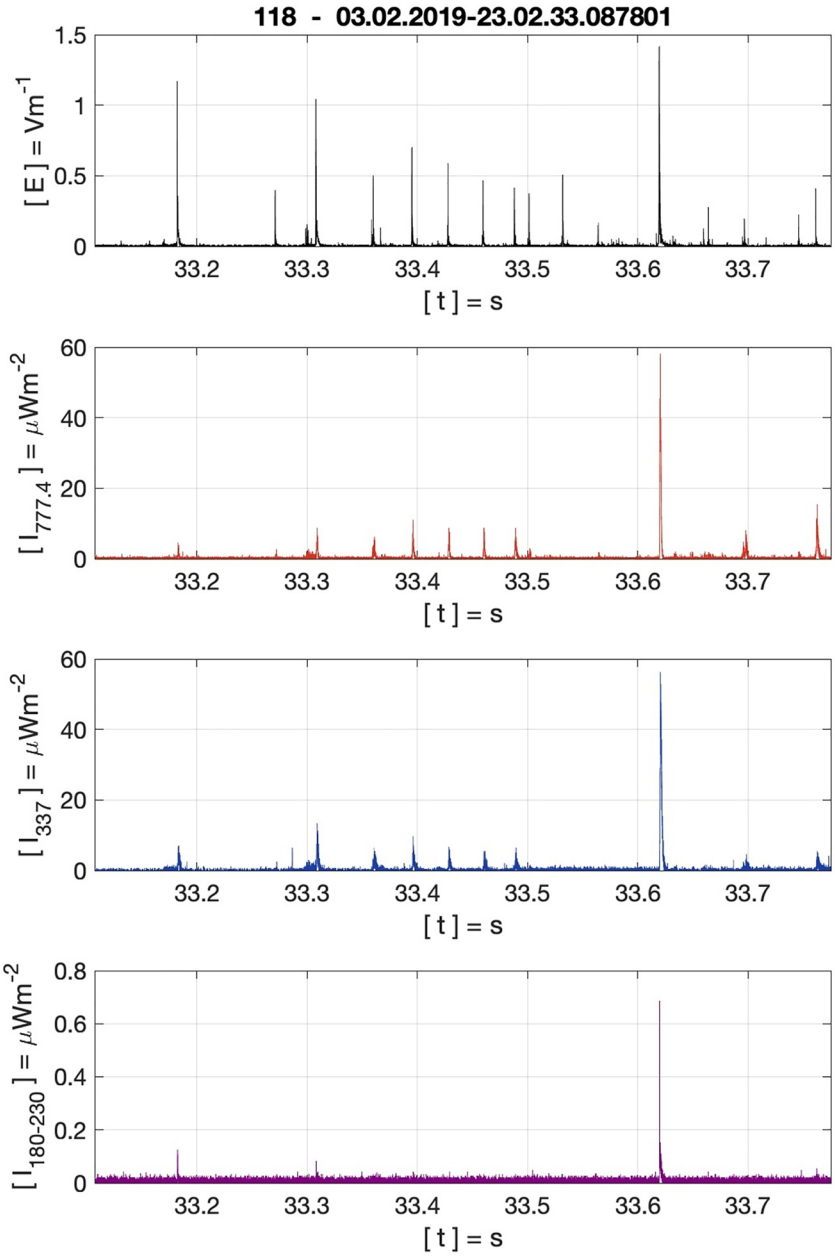

Figure 4. Comparison of vertical electric field recordings with optical photometers recordings of Modular Multispectral Imaging Array (MMIA) on the International Space Station (ISS). (upper panel) The envelope of the electric recordings exhibits numerous pulses, most of which are associated with optical pulses recorded by the photometers (lower three panels) which measured red, blue, and UV wavelengths. See text for details.

model. According to the time delays Δt_1 and Δt_2, the corresponding distance differences ΔD_1 and ΔD_2 can be calculated under the assumption that the wave propagation velocity is equal to the speed of light c such that $\Delta D_1 = c\Delta t_1$ and $\Delta D_2 = c\Delta t_2$.

5.1. Spherical Model

The wave propagation models are illustrated in Figures 6b and 6c. These two models are combined to estimate the ionospheric height and the source event height. The angle α can be calculated using

$$\alpha = \frac{d}{r}, \tag{1}$$

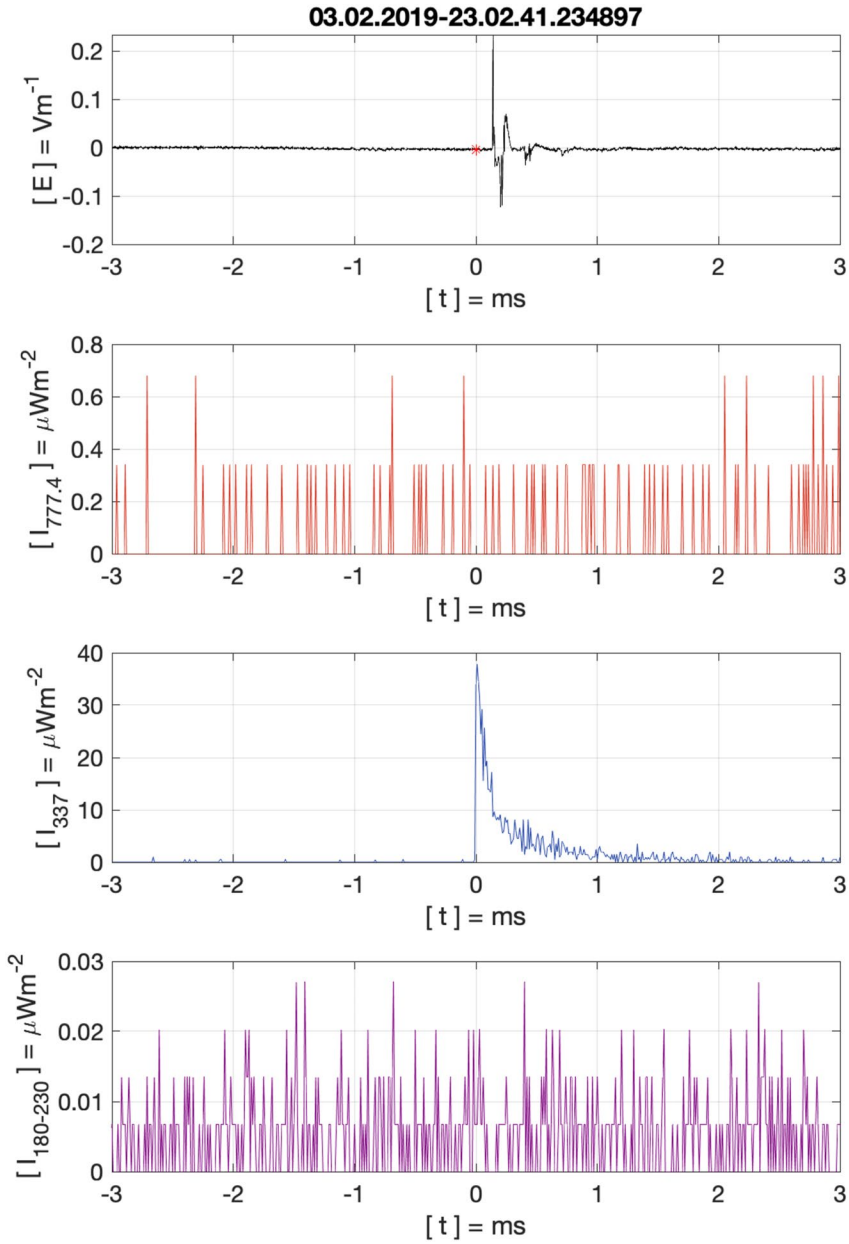

Figure 5. All records are referenced to the occurrence time of a lightning flash reported by Earth Networks Total Lightning Network (ENTLN; upper panel, red star). The vertical electric field waveform within the dashed lines is shown in Figure 6a in more detail.

where d is the distance between the source event and the receiver, a spherical Earth model is adopted in this study, and the distance between the receiver and the source is 766.4 km as reported by ENTLN, where $r = 6{,}371$ km is the equivolumetric radius of the Earth.

5.1.1. Ionospheric Reflection Model

This model is suitable for the skywaves that are first reflected by the ionosphere (Figure 6b). Different combinations of ionospheric height h_i and source event height h_s are simulated to calculate the first skywave ionospheric reflection path $x_1 + x_2$, and the second skywave ionospheric reflection path $x_3 + 2 \times x_4 + x_5$. Then, the distance difference between the first and second skywave ionospheric reflection paths can be calculated and compared to the measured distance difference ΔD_1. As the ionospheric reflection height during the nighttime is stable, in this work, we assume that the ionospheric height over the wave propagation path is constant. For a set composed

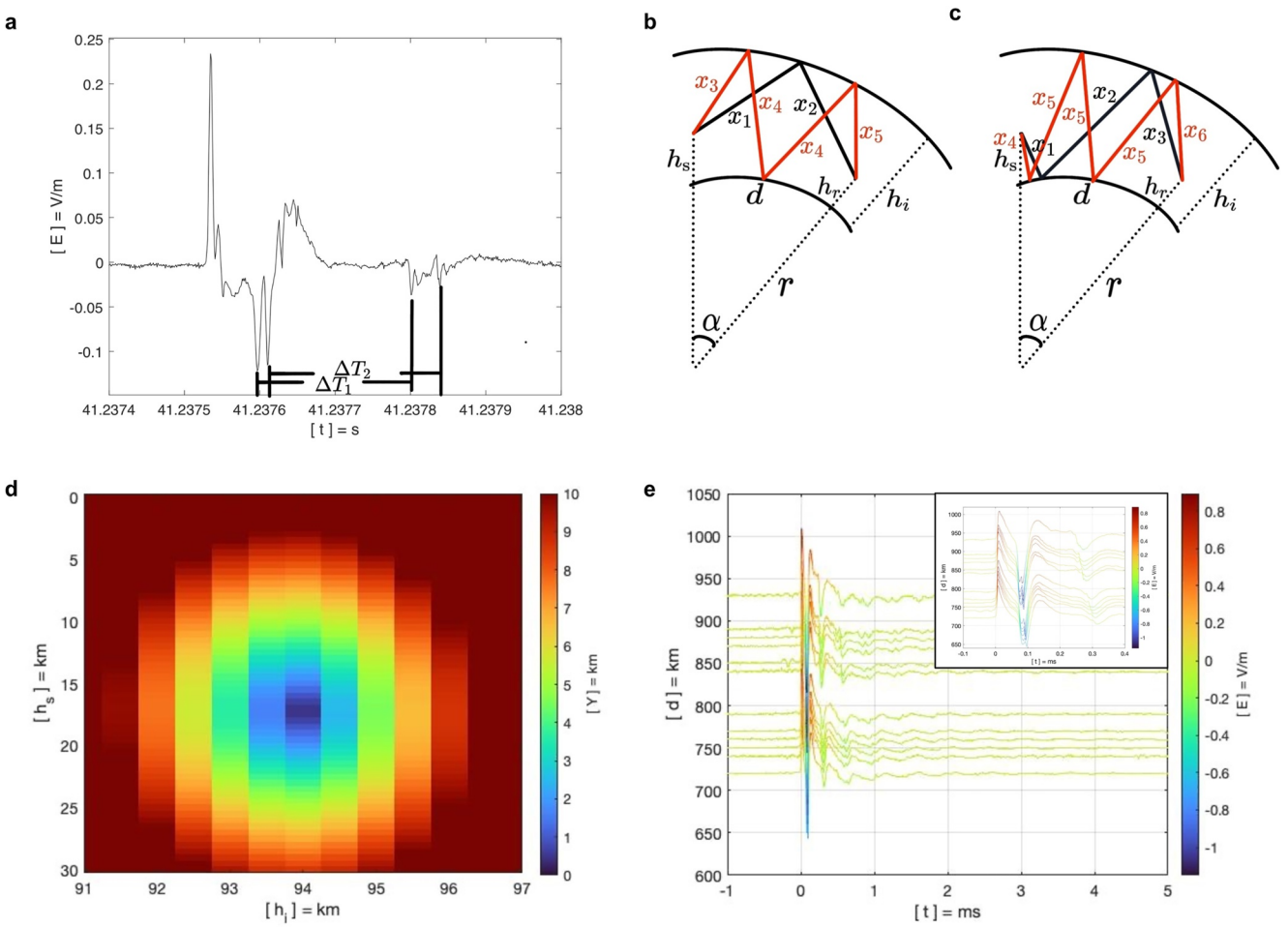

Figure 6. Determination of the height of the blue discharge. (a) The consecutive maxima of the electric field recordings are used to determine the height of the ionosphere and height of the blue discharge. The time difference ΔT_1 is associated with the model in (b), and time difference ΔT_2 is associated with the model in (c). The peak of the waveform corresponds to the ground wave. For ΔT_1 and ΔT_2, the rising edges correspond to the first skywave, while the falling edges correspond to the second skywave. (b, c) Observation geometry and path of the consecutive skywaves used to determine the source height h_s which are observed with a receiver at the height h_r. The first skywave propagation paths are marked in black, while the second skywave propagation paths are marked in red. (d) The height of the blue discharge and the ionospheric height are inferred from simulations for various parameter combinations which offers an assessment of the relative uncertainty of the estimates. (e) The waveform table calculated from many negative lightning discharges exhibits consecutive skywaves which are used to calculate an average ionospheric height ~93.4 km. For each distance bin, an averaged amplitude waveform is plotted with its *y*-axis entered at its corresponding distance bin where the color scale represents its electric field.

of the ionospheric height h_i and the source event height h_s, the ionospheric reflections can be calculated using Equations A1–A5 in Appendix A, where d is the propagation distance, h_r is the receiver height (i.e., 1.341 km), r is the Earth radius, and α is the center angle. Equations A1, A3, and A4 mean the incidence angle is equal to the reflection angle. Equations A2 and A5 indicate the angle enclosed by the ionospheric propagation path equals α.

The difference between the observed and simulated results in ionospheric reflection model Y_1 is given by

$$Y_1 = x_1 + x_2 - (x_3 + 2x_4 + x_5) + \Delta D_1. \quad (2)$$

5.1.2. Ground Reflection Model

This model is suitable for the skywaves that are first reflected by the ground (Figure 6c). Different combinations of ionospheric height h_i and source event height h_s are simulated to calculate the first skywave ground reflection path $x_1 + x_2 + x_3$, and the second skywave ground reflection path $x_4 + 3 \times x_5 + x_6$. Then, the distance difference between the first and second skywave ground reflection paths can be calculated and compared to the measured distance difference ΔD_2. For a set composed of the ionospheric height h_i and the source event height

h_s, the ground reflections can be calculated using Equations A6–A11 in Appendix A, where d is the propagation distance, h_r is the receiver height, r is the Earth radius, and α is the center angle. Equations A6, A7, A9, and A10 mean that the incidence angle is equal to the reflection angle. Equations A8 and A11 indicate the angle enclosed by the ionospheric propagation path equals α.

The difference between the observed and simulated results in ground reflection model Y_2 is given by

$$Y_2 = x_1 + x_2 + x_3 - (x_4 + 3x_5 + x_6) + \Delta D_2. \tag{3}$$

For a simulated ionospheric height and source event height pair, the overall distance uncertainty Y is

$$Y = \sqrt{\frac{Y_1^2 + Y_2^2}{2}}. \tag{4}$$

The overall distance uncertainties Y are shown in Figure 6d based on different simulated ionospheric heights and source event heights. The best fitting results should provide a minimum overall distance uncertainty Y. The best matched ionospheric height is 95.0 km, and the event source height is 17.4 km.

A sensitivity analysis for the timing is carried out to constrain the simulations. With a timing uncertainty assumed from the electric field measurements of ±3 μs, the ionospheric height is within a range from 94.5 to 95.5 km, that is, ∼95.0 km (±0.5) km, and the source height is between 16.0 and 18.8 km, that is, ∼17.4 km (±1.4) km. With a timing uncertainty of ±1 μs, the ionospheric height is between 94.8 and 95.2 km, that is, ∼95.0 km (±0.2) km, and the source height is between 16.9 and 17.9 km, that is, ∼17.4 km (±0.5) km.

5.2. Ionospheric Height From Amplitude Waveform Bank

A waveform bank consists of distance-dependent averaged waveforms, and it is a useful tool to investigate lightning waveform characteristics (e.g., Bai & Füllekrug, 2022; Z. Liu et al., 2018; Said et al., 2010). The waveform bank is used here to calculate the ionospheric height. The lightning location used to calculate the amplitude waveform bank is provided by SALDN data. In this amplitude waveform bank in Figure 6e, only negative CGs are included to mitigate the larger positive peak currents and each waveform is scaled to the ground wave maximum. The distance range of the amplitude waveform bank is 720–930 km, which covers the propagation distance of the blue discharge event, which is 766.4 km. Therefore, the ionospheric height determined by the amplitude waveform bank can be used as a reference to the ionospheric height determined by the blue discharge event. The distance bins for the amplitude waveform bank are separated by 10 km. All the waveforms that fall ±5 km around this distance bin are averaged to one waveform to represent this distance. Each distance bin needs to include more than 100 events to produce a reliable averaged waveform, which explains the gaps shown in Figure 6e. The skywave propagation model used here is modified from the model created by Laby et al. (1940) and Schonland et al. (1940). The receiver height is considered. Based on the time differences between the first and second skywaves, the ionospheric heights are calculated for different distances with a mean value of ∼93.4 km. This result matches well with the ionospheric height determined from the measurements of the blue discharge event as explained in the previous section.

6. Estimation of the Source Altitude From the Optical Pulse

The altitude of the flash can also be determined from the analysis of the optical pulse observed in the 337 nm photometer. Following the work of Luque et al. (2020) and Soler et al. (2020), we can estimate the height of the blue discharge from the optical pulse shape with the assumption that the source is prompt and located at a cloud depth L below the top of a planar cloud. Rewriting Equation 1 from Soler et al. (2020), which was originally introduced by Krapivsky et al. (2010), with different variables and for an instantaneous source at $t = 0$, we have

$$I(t) = \frac{I_m}{\left(\frac{6Dt}{L^2}\right)^{\frac{3}{2}}} e^{\frac{3}{2} - \frac{L^2}{4Dt} - \gamma t}, \tag{5}$$

where I is the photon intensity, I_m is the maximum photon intensity, D is the diffusion coefficient for photon scattering, and γ is photon absorption frequency. For the 337 nm wavelength, the absorption frequency varies between 10^{-2} and 10^{-1} s^{-1} (Soler et al., 2020) and it is reasonable to neglect the absorption for pulses of a few ms duration. In this case, the equations becomes

$$I(t) = \frac{I_m}{\left(\frac{6Dt}{L^2}\right)^{\frac{3}{2}}} e^{\frac{3}{2} - \frac{L^2}{4Dt}}. \quad (6)$$

The maximum of the pulse is reached at the time $L^2/6D$ and the photon flux depends only on L^2/Dt, the 10%–90% rise time T_r is given by $T_r = 0.0742\ L^2/D$. The cloud depth L is then the square root of the rise time given by $L = \sqrt{\frac{D \cdot T_r}{0.0742}} = 4.041 \cdot 10^4 / r\sqrt{T_r / N_d}$, where N_d is the cloud particle concentration and r the radius of the particles. Subtracting this from the cloud top altitude gives an estimate of the event altitude.

The third panel of Figure 5 gives the light curve from the 337 nm photometer, a direct measurement the rise time by linear interpolation would give 9 μs which is below the 10 μs period of the photometer sampling. To measure the true rise time of a light pulse that follows Equation 5, we have modeled the sampling of the equation by the photometer, simulating the light integration done by the instrument in every sample for different starting times in 100–110 μs and rise times in 0–100 μs in Equation 5. We found a perfect match during the rising period between the simulated sampling of the pulse and the photometer response for only one pulse having a start time 101.1 μs and a true rise time of 5.5 μs. The match is given in supplementary material as Figure S1 in Supporting Information S1, in which we give plots of the pulse from Equation 5 together with its simulated sampling and the ASIM photometer response, the sampling point matches perfectly at 100, 110, and 120 μs and we take the value of 5.5 μs as best estimate. We also note that the rise time is associated with a time constant $L^2/4D$ of 18.5 μs. With a cloud top altitude between 13.3 and 16.7 km from Figure 2, assuming a cloud particle concentration of 10^8 m^{-3} and a particle radius of 15 μm corresponding to a photon mean free path of 7 m (Soler et al., 2020), the cloud depth is 0.64 km. To estimate the uncertainty, one can assume a cloud particle concentration from 10^7 to 10^8 m^{-3} (Knollenberg et al., 1993) and a particle radius from 10 to 20 μm (Bennartz, 2007) to get a cloud depth range of 0.5–3.1 km (see Figure 7a) and an event altitude of 10.2–16.1 km (see Figure 7b). We note that the estimation of the maximum altitude with this method is at the bottom edge of the altitude range of 16.0–18.8 km estimated by the radio measurements. The uncertainty range of the cloud particle concentration and particle radius will be discussed further in the next section.

7. Discussion

The blue discharge was observed during the vertical development of a thunder cell embedded within a convective line of several hundreds of kilometers length. This cell exhibited a cloud top height ∼16.4 km with a small overshoot above the tropopause (∼150 m in height and one pixel in lateral extent) according to the MSG/SEVIRI observation. In Section 3, by combining the uncertainty about the CTT estimation (2.5°C) and that about the location from ASIM imagery (5 km), we estimated the altitude of the blue discharge between 13.3 and 16.7 km.

However, according to the resolution of the SEVIRI radiometer in the region (3.5 km × 3.5 km for one pixel) and the small area with lower CTT, it is difficult to estimate with large accuracy the CTT and therefore its altitude. In order to have an independent estimate of the cloud top altitude, we use S-band Doppler radar measurements at Irene, South Africa (28.21°E, 25.91°S), ∼66 km away from the cell location. Figure 8 displays the composite image made with 11 radar beam elevations from 0.5° to 22.3° centered in time around 23:04:51 UTC. Figure 8a shows the maximum reflectivity vertically found within the cloud, while Figure 8b shows a reconstituted vertical cross section along the 32 km long red dashed line in Figure 8a. Furthermore, Figure 8c shows a zoom of the main cell corresponding to the white frame in Figure 8a. As in other studies of altitude discharges, the high region of the thundercloud is not completely scanned by the radar beam and the cloud top may not be intercepted by the radar beam between two neighboring scan elevations (Dimitriadou et al., 2022). When the elevation angle is large between two successive scans at different elevation angles, there is a region of the cloud that is not covered by the radar beam. Thus, the vertical cross section cannot completely account for the overshoot above 16 km in the present case. The reflectivity is only reported at given distances (circles around the radar) that do not correspond to the maximum of the reflectivity and therefore to the convective core. Indeed, values of reflectivity up to 33 dBZ are reported at a level very close to 16 km in the region of the storm indicated by the white arrow which can be considered as the region of the overshoot. Figure 8c shows that the blue discharge indicated by the black cross is located very close to this region, also indicated by the white arrow on the dashed line (<3 km). It confirms the observation made from Figure 1f where the blue discharge was located very close to the minimum CTT. The location of blue corona discharges detected by ASIM above two regions of the same thunderstorm in northern

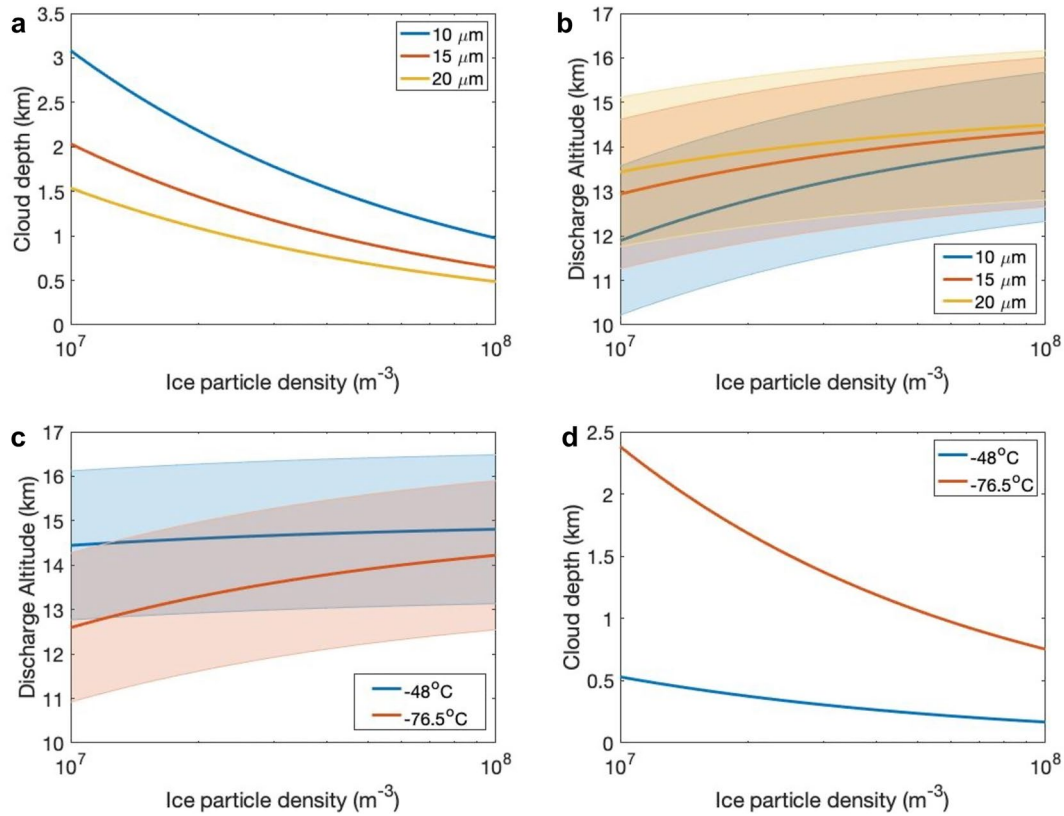

Figure 7. (a) Estimate of the cloud depth as a function of the ice particle density for three constant ice particle radius: 10, 15, and 20 μm. (b) Estimate of the event altitude as a function of the ice particle density for three constant ice particle radius: 10, 15, and 20 μm. (c) Estimate of the cloud depth as a function of the ice particle density for two ice particle size distribution corresponding to −48°C and −76.5°C. (d) Estimate of the event altitude as a function of the ice particle density for two ice particle size distribution corresponding to −48°C and −76.5°C.

Australia was considered by Dimitriadou et al. (2022). These blue corona discharges were produced close to the highest regions of the thunderclouds which reached to altitudes above the tropopause at 17 km in a more tropical region when compared to the present case and with CAPE values of 4 kJ kg^{-1}. The radar also could not detect the cloud tops in this case, only giving values of ∼22 dBZ at 17 km. In the present case, with values of 30–33 dBZ observed at an altitude close to 16 km, it is thought that the cloud top was locally above 16 km. Indeed, according to the study of tropical "hot towers" by Williams et al. (1992), the 30 dBZ reflectivity can reach 16–17 km in the towers near cloud tops.

The blue discharge altitude is also estimated by the electric field recordings of skywave arrival times. Except for the sensitivity analysis based on the electric field timing, which gives the event altitude uncertainty range of 16.0–18.8 km, the height uncertainty is also given by a sensitivity analysis based on the altitude determination algorithm. This method simulates different ionospheric heights and blue discharge heights to find a minimum root mean square value of the distance differences of the propagation along two ionospheric reflection paths Y_1 and two ground reflection paths Y_2. The time uncertainty is not considered here. It can be seen from Figure 6d that the height uncertainty for the blue discharge is estimated to between 15.5 and 19.0 km with a distance uncertainty of 1 km for the distance difference Y (defined in Equation 4). The distance difference Y is a measurement related to the propagation path, which is ∼766.4 km, therefore an uncertainty range of 1 km corresponds to a relative uncertainty of ∼0.1%.

We now look further at the altitude determination from the optical pulse from the blue discharge event. From Figure 7, it can be noted that the uncertainty comes mainly from two origins that can be discussed. The first is the ice crystal size and second the ice crystal density. The ice particle size is assumed to be constant for the three curves given in Figure 7a which is a strong hypothesis that can be relaxed by choosing a particle size distribution

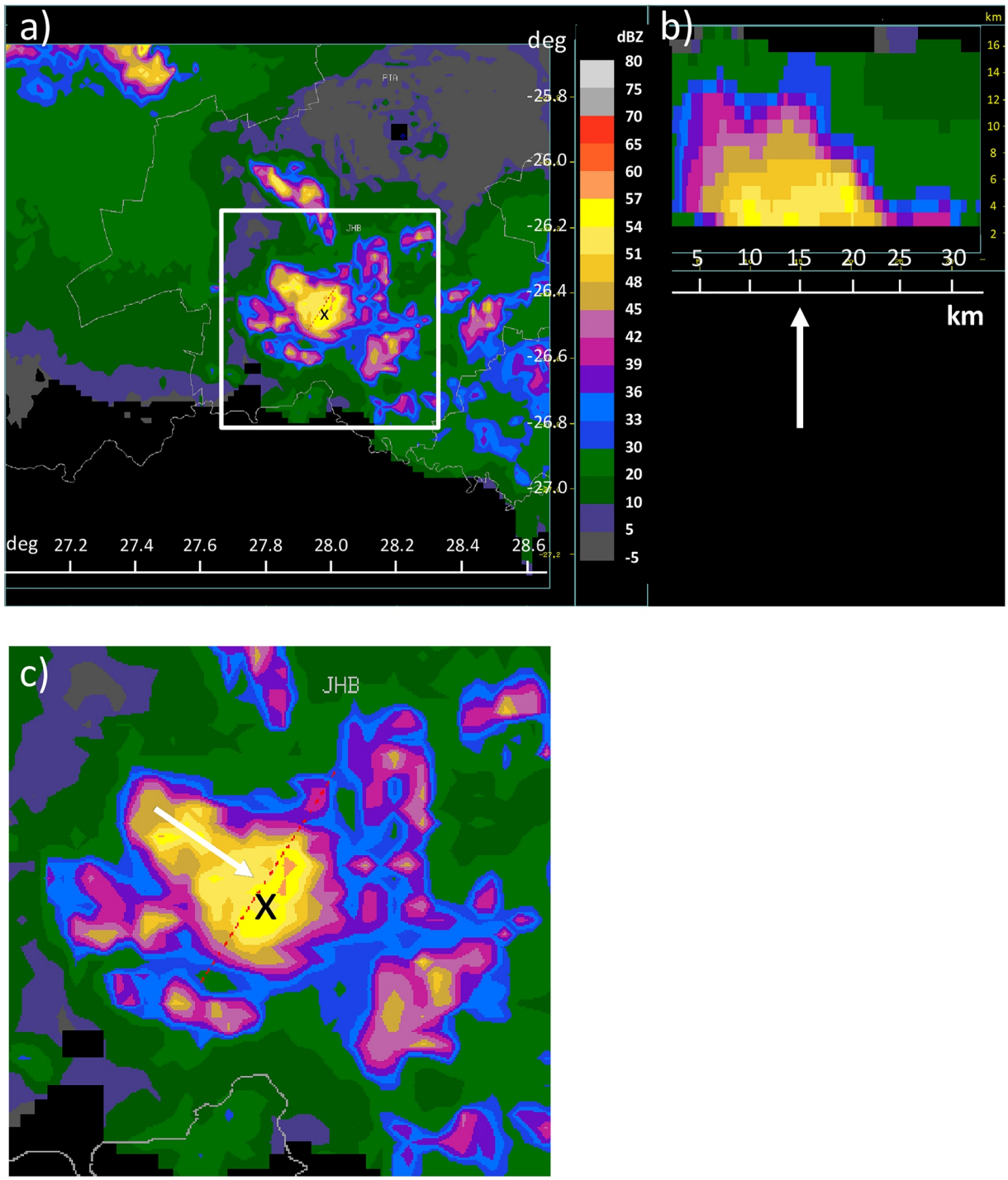

Figure 8. Radar composite image of the cell producing the blue discharge, at 23:04:51 UTC. (a) Horizontal cross section with the maximum reflectivity (dBZ) in the column; (b) vertical cross section along the red dashed line in (a); (c) zoom into the white frame included in (a). The black cross indicates the blue discharge location (27.97°E; 26.47°S). The white arrow in (b) and (c) indicates the location of the maximum altitude with the highest reflectivity observed along the vertical cross section.

(PSD) that is more realistic to the cloud top ice particle composition. Following Heymsfield et al. (2013, Equation 6), the PSD can be fitted to a gamma distribution of the form $N(D) = N_0 D^{\mu} e^{-\lambda D}$ where μ is the dispersion, λ is the slope, and N_0 is the intercept (here, chosen such that the PSD is normalized) and the parameters λ and μ can be expressed as a function of the temperature (Montanyà et al., 2021).

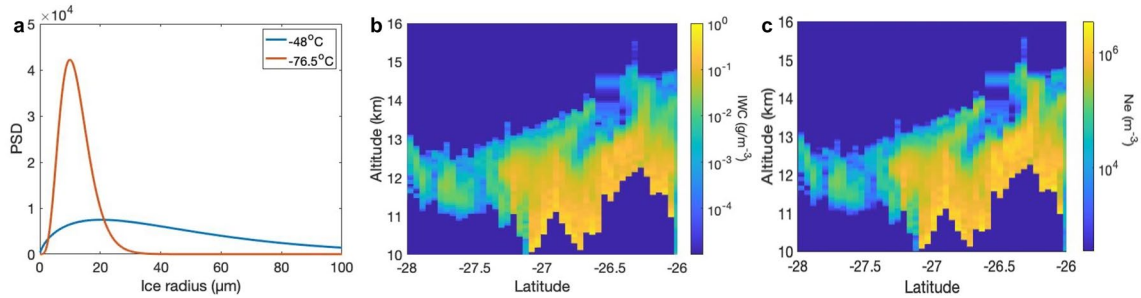

Figure 9. (a) Normalized particle size distribution (PSD) for ice crystals temperature at −48°C and −78.5°C; (b) ice water content (IWC) and ice crystal density (c) as a function of the altitude along the track of CALIPSO recorded at about 23:35 UTC.

To estimate the temperature range between the discharge origin and the cloud top, we anticipate a maximal cloud depth of about 2 km. It corresponds to an altitude range of 11.3–16.7 km and a temperature range between −48°C and −76.5°C. According to Heymsfield et al. (2013), at those temperatures λ varies then between 176 and 2,300 cm^{-1} and μ varies between 0.71 and 4.6, giving the normalized PSDs plotted in Figure 9a. Knowing the PSD as a function of the temperature makes it then possible to calculate the key parameters affecting the propagation of light in the cloud. For a density varying between 10^7 and 10^8 m^{-3} and a temperature varying between −48°C and −76.5°C, the mean free path varies between 0.45 and 90 m, the absorption frequency between 49.6 and 0.37 s^{-1}, and the diffusion coefficient between 3.7×10^9 and 7.9×10^{10} m^2/s. With a true rise time of 5.5 μs and with an ice particle density in the range of 10^7–10^8 m^{-3}, the cloud depth is now estimated between 0.2 and 2.4 km from Figure 7c and the discharge altitude between 10.9 and 16.5 km from Figure 7d.

The last parameter to discuss for the estimation of the discharge altitude is the particle ice density. We looked at the Cloud-Aerosol Lidar and Infrared Pathfinder Satellite Observations, that is, CALIPSO, satellite data (e.g., M. A. Vaughan et al., 2004; Winker et al., 2003) which allow to measure the ice composition at cloud top heights. The CALIPSO track is marked as a red dashed line in Figure 1f. Unfortunately, it flew over another thunderstorm cell centered at the longitude and latitude 28.75°E and 26.5°S. However, it is close enough to the cell from which the blue discharge originated such that it is reasonable to assume that the thermodynamical composition of the cell is similar, and that the ice PSD follows the same dependency with the temperature. The CALIPSO track is indicated in Figure 1f by a red line corresponding to a pass ∼23:35 UTC. CALIPSO allows to estimate the ice water content (IWC; Delanoë & Hogan, 2010) which is given along the track in Figure 9b. The IWC of the cell observed by CALIPSO is discussed here for the purposes of determining the ice crystal density, which will be used to further estimate the ice crystal density of the cell which produces the blue discharge.

We note that the IWC varies between 0.02 and 1 g/m^3 below a small overshoot that was measured ∼23:34:50 UTC. Following Heymsfield et al. (2013), the IWC is given by $IWC = \int_D n_{ice} N(D) m(D) dD$, where n_{ice} is the ice crystal density, $N(D)$ is the PSD, and $m(D)$ is the ice crystal mass relationship developed by Schmitt and Heymsfield (2009) $m(D) = 0.91 \frac{\pi}{6} D^3 e^{-94D}$ with D in cm and m in g. The IWC allows therefore to estimate the ice crystal density which is given in Figure 9c and we can see that the ice crystal density varies between 4×10^5 and 2.8×10^6 m^{-3} which appears low when compared to the estimate used in the preceding section and we remind the reader it corresponds to another cell than the one from which the blue discharge originated.

The movie "CellEvolution.avi" in the supplementary material gives the temporal evolution in time of the cells. It is noted that the CTT of the cell observed by CALIPSO ∼23:35 UTC is −67°C, that is, ∼5°C warmer than the cell from which the discharge occurs. The cell observed by CALIPSO is therefore below the tropopause. From the reflectivity presented in Figure 8, we can also note that the radar reflectivity reaches maximum values of 58.5 dBz for the cell with the blue discharge and 46.5 dBZ for the cell observed by CALIPSO. The difference in dBZ is similar to the difference in radar reflectivity between a mature overshooting top and a decaying one, for example, as observed by Homeyer and Kumjian (2015, Figure 11). The movie "CellEvolution.avi" also indicates that the cell with the blue discharge is in a higher level of overshooting maturity than the cell observed by CALIPSO. The first cell is 15 min after the maximum of its overshooting phase and the second does not overshoot at all. Such difference of reflectivity can be related to a ratio of ice particle density assuming the reflectivity is directly proportional to it, and we find that the ice crystal density from the cell producing the discharge is about

30 times higher than that of the cell observed by CALIPSO. Finally, we find that the ice density for the cell that produced the blue discharge can be estimated to be between 1.2×10^7 and 8.4×10^7 m^{-3}. Furthermore, and even if the measurement of cloud tops ice density is difficult to obtain, we can note that this range is in good agreement with Krämer et al. (2020) and Protat et al. (2011) which report ice particle densities that reach values as high as 3×10^7 and 10^8 m^{-3}, respectively. Those findings coincide with the range we have chosen in the preceding section and the corresponding altitude range we obtained for the altitude of the discharge from the optical measurement of ASIM, that is, 10.9–16.5 km.

This work enables a thorough estimation of measurement uncertainties of an exemplary blue discharge event height, while the parameters are chosen to be consistent because only one event is available to us. The parameters that affect the uncertainty are CTT estimation, location, reflectivity, distance, ice crystal size, and ice crystal density, which are thoroughly discussed in this section.

8. Summary and Conclusions

The ASIM/MMIA overpass in South Africa described in this report enables an extension of previous results with a focus on the comparison between space-based optical observations and ground-based electric field recordings.

A strong link between optical and electric field observations was found for the blue PMT pulses which are associated with lightning discharges reported by lightning detection networks. One question of particular interest in this context is whether the height of the blue discharges can be determined with significant confidence. There are three sources of height information which have been used, that is, the cloud top height inferred from geostationary satellite imagery, the pulse height determination from skywave arrival times, and the height estimation from the optical recordings.

The calculated cloud top height is 13.3–16.7 km. From the radio recordings, the altitude of this blue discharge event is 17.4 km with uncertainty range of 16.0–18.8 km by using a spherical Earth model. The ionospheric height calculated using the same model is 95.0 km, which is consistent with that determined from the waveform bank of CG discharges (93.4 km). The height estimation derived from the rising edge of the blue optical emission is between 10.9 and 16.5 km.

Besides studies of selected events, as pursued in this report, this unique and rich data collected by MMIA on ASIM could also be used to study the statistical properties of many events, for example, a comparison of peak pulse intensities and rise times of electric field recordings associated with many blue and/or red PMT pulses and their association with reports from lightning detection networks.

Appendix A: Equations of Source and Ionospheric Reflection Heights Determination

Equations A1 and A2 refer to the ionospheric reflection model in Figure 6b. For the path $x_1 + x_2$, the incidence angle into the ionosphere equals to the reflection angle in Equation A1:

$$\frac{x_1^2 + (h_i + r)^2 - (h_s + r)^2}{2x_1(h_i + r)} = \frac{x_2^2 + (h_i + r)^2 - (h_r + r)^2}{2x_2(h_i + r)}. \tag{A1}$$

For the first skywave propagation path, the center angle α can be seen as two portions: portion 1 is enclosed by $h_s + r$ and $h_i + r$, and portion 2 is enclosed by $h_i + r$ and $h_r + r$:

$$\alpha = \cos^{-1}\left(\frac{(h_s + r)^2 + (h_i + r)^2 - x_1^2}{2(h_s + r)(h_i + r)}\right) + \cos^{-1}\left(\frac{(h_r + r)^2 + (h_i + r)^2 - x_2^2}{2(h_r + r)(h_i + r)}\right). \tag{A2}$$

For the path $x_3 + x_4$ and the path $x_4 + x_5$, the incidence angle into the ionosphere equals to the reflection angle in Equations A3 and A4

$$\frac{x_3^2 + (h_i + r)^2 - (h_s + r)^2}{2x_3(h_i + r)} = \frac{x_4^2 + (h_i + r)^2 - r^2}{2x_4(h_i + r)}, \tag{A3}$$

$$\frac{x_4^2+(h_i+r)^2-r^2}{2x_4(h_i+r)}=\frac{x_5^2+(h_i+r)^2-(h_r+r)^2}{2x_5(h_i+r)}. \tag{A4}$$

For the second skywave propagation path, the center angle α can be seen as four portions: portion 1 is enclosed by h_s+r and h_i+r, portion 2 and portion 3 are both enclosed by h_i+r and r, and portion 4 is enclosed by h_i+r and h_r+r:

$$\alpha=\cos^{-1}\left(\frac{(h_s+r)^2+(h_i+r)^2-x_3^2}{2(h_s+r)(h_i+r)}\right)+2\cos^{-1}\left(\frac{r^2+(h_i+r)^2-x_4^2}{2r(h_i+r)}\right)+\cos^{-1}\left(\frac{(h_r+r)^2+(h_i+r)^2-x_5^2}{2(h_r+r)(h_i+r)}\right). \tag{A5}$$

Equations A6–A10 refer to the ground reflection model in Figure 6c. For the path x_1+x_2, the incidence angle into the ground equals to the reflection angle in Equation A6:

$$-\frac{x_1^2+r^2-(h_s+r)^2}{2x_1r}=-\frac{x_2^2+r^2-(h_i+r)^2}{2x_2r}. \tag{A6}$$

For the path x_2+x_3, the incidence angle into the ionosphere equals to the reflection angle in Equation 4:

$$\frac{x_2^2+(h_i+r)^2-r^2}{2x_2(h_i+r)}=\frac{x_3^2+(h_i+r)^2-(h_r+r)^2}{2x_3(h_i+r)}. \tag{A7}$$

For the first skywave propagation path, the center angle α can be seen as three portions: portion 1 is enclosed by h_s+r and r, portion 2 is enclosed by h_i+r and r, and portion 3 is enclosed by h_i+r and h_r+r:

$$\alpha=\cos^{-1}\left(\frac{(h_s+r)^2+r^2-x_1^2}{2r(h_s+r)}\right)+\cos^{-1}\left(\frac{r^2+(h_i+r)^2-x_2^2}{2r(h_i+r)}\right)+\cos^{-1}\left(\frac{(h_i+r)^2+(h_r+r)^2-x_3^2}{2(h_i+r)(h_r+r)}\right). \tag{A8}$$

For the path x_4+x_5, the incidence angle into the ground equals to the reflection angle in Equation A9:

$$-\frac{x_4^2+r^2-(h_s+r)^2}{2x_4r}=-\frac{x_5^2+r^2-(h_i+r)^2}{2x_5r}. \tag{A9}$$

For the path x_5+x_6, the incidence angle into the ionosphere equals to the reflection angle in Equation A10:

$$\frac{x_5^2+(h_i+r)^2-r^2}{2x_5(h_i+r)}=\frac{x_6^2+(h_i+r)^2-(h_r+r)^2}{2x_6(h_i+r)}. \tag{A10}$$

For the second skywave propagation path, the center angle α can be seen as five portions: portion 1 is enclosed by h_s+r and r, portions 2–4 are all enclosed by h_i+r and r, and portion 5 is enclosed by h_i+r and h_r+r:

$$\alpha=\cos^{-1}\left(\frac{(h_s+r)^2+r^2-x_4^2}{2r(h_s+r)}\right)+3\cos^{-1}\left(\frac{r^2+(h_i+r)^2-x_5^2}{2r(h_i+r)}\right)+\cos^{-1}\left(\frac{(h_r+r)^2+(h_i+r)^2-x_6^2}{2(h_r+r)(h_i+r)}\right). \tag{A11}$$

All the equations used here are according to the cosine rule.

Data Availability Statement

The data used for this publication will be available from https://doi.org/10.15125/BATH-01103.

References

Adachi, T., Sato, M., Ushio, T., Yamazaki, A., Suzuki, M., Kikuchi, M., et al. (2016). Identifying the occurrence of lightning and transient luminous events by nadir spectrophotometric observation. *Journal of Atmospheric and Solar-Terrestrial Physics*, *145*, 85–97. https://doi.org/10.1016/j.jastp.2016.04.010

Aminou, D. M. A., Jacquet, B., & Pasternak, F. (1997). Characteristics of the Meteosat Second Generation (MSG) radiometer/imager: SEVIRI. *Sensors, Systems, and Next-Generation Satellites*, *3221*, 19–31. https://doi.org/10.1117/12.298084

Bai, X., & Füllekrug, M. (2022). Coherency of lightning sferics. *Radio Science*, *57*, e2021RS007347. https://doi.org/10.1029/2021RS007347

Acknowledgments
The work of X.B. was sponsored by URSA under the project Grant EA-EE1250. The work of M.F., D.M., and M.K. was sponsored by the Royal Society (UK) Grant NMG/R1/180252 and the Natural Environment Research Council (UK) under Grants NE/L012669/1 and NE/H024921/1. This project has received funding from the European Union's Horizon 2020 research and innovation program under the Marie Sklodowska-Curie Grant agreement 722337. ASIM is a mission of the European Space Agency (ESA) and is funded by ESA and by national grants of Denmark, Norway, and Spain. The ASIM Science data center is supported by ESA PRODEX contracts C 4000115884 (DTU) and 4000123438 (Bergen). The work of V.R. was funded by the Ministerio de Ciencia e Innovación Grant PID2019-109269RB-C41. This study was supported by the Research Council of Norway under contract 223252/F50 (CoE). The authors thank the French AERIS/ICARE Data and Services Center which provided MSG/SEVIRI data for cloud top temperature. They thank the European Copernicus/ECMWF data center, the US NCEP/NCAR, and NOAA for providing meteorological reanalysis. They thank also the SALDN, ENTLN, and GLD360 for providing the lightning and radar data. The authors wish to thank Simon Ghilain for initiating this work and the reviewers for their assistance to improve the quality of the manuscript.

Bennartz, R. (2007). Global assessment of marine boundary layer cloud droplet number concentration from satellite. *Journal of Geophysical Research*, *112*, D02201. https://doi.org/10.1029/2006JD007547

Blanc, E., Farges, T., Roche, R., Brebion, D., Hua, T., Labarthe, A., & Melnikov, V. (2004). Nadir observations of sprites from the International Space Station. *Journal of Geophysical Research*, *109*, A02306. https://doi.org/10.1029/2003JA009972

Brunner, K. N., & Bitzer, P. M. (2020). A first look at cloud inhomogeneity and its effect on lightning optical emission. *Geophysical Research Letters*, *47*, e2020GL087094. https://doi.org/10.1029/2020gl087094

Chanrion, O., Neubert, T., Lundgaard Rasmussen, I., Stoltze, C., Tcherniak, D., Jessen, N. C., et al. (2019). The Modular Multispectral Imaging Array (MMIA) of the ASIM payload on the International Space Station. *Space Science Reviews*, *215*(4), 28. https://doi.org/10.1007/s11214-019-0593-y

Chanrion, O., Neubert, T., Mogensen, A., Yair, Y., Stendel, M., Singh, R., & Siingh, D. (2017). Profuse activity of blue electrical discharges at the tops of thunderstorms. *Geophysical Research Letters*, *44*, 496–503. https://doi.org/10.1002/2016GL071311

Chen, A. B., Kuo, C.-L., Lee, Y.-J., Su, H.-T., Hsu, R.-R., Chern, J.-L., et al. (2008). Global distributions and occurrence rates of transient luminous events. *Journal of Geophysical Research*, *113*, A08306. https://doi.org/10.1029/2008JA013101

Chern, J. L., Hsu, R. R., Su, H. T., Mende, S. B., Fukunishi, H., Takahashi, Y., & Lee, L. C. (2003). Global survey of upper atmospheric transient luminous events on the ROCSAT-2 satellite. *Journal of Atmospheric and Solar-Terrestrial Physics*, *65*(5), 647–659. https://doi.org/10.1016/S1364-6826(02)00317-6

Chou, J.-K., Hsu, R.-R., Su, H.-T., Chen, A. B.-C., Kuo, C.-L., Huang, S.-M., et al. (2018). ISUAL-observed blue luminous events: The associated sferics. *Journal of Geophysical Research: Space Physics*, *123*, 3063–3077. https://doi.org/10.1002/2017JA024793

Delanoë, J., & Hogan, R. J. (2010). Combined CloudSat-CALIPSO-MODIS retrievals of the properties of ice clouds. *Journal of Geophysical Research*, *115*, D00H29. https://doi.org/10.1029/2009JD012346

Dimitriadou, K., Chanrion, O., Neubert, T., Protat, A., Louf, V., Heumesser, M., et al. (2022). Analysis of blue corona discharges at the top of tropical thunderstorm clouds in different phases of convection. *Geophysical Research Letters*, *49*, e2021GL095879. https://doi.org/10.1029/2021GL095879

Füllekrug, M. (2010). Wideband digital low-frequency radio receiver. *Measurement Science and Technology*, *21*(1), 015901. https://doi.org/10.1088/0957-0233/21/1/015901

Füllekrug, M., Nnadih, S., Soula, S., Mlynarczyk, J., Stock, M., Lapierre, J., & Kosch, M. (2019). Maximum sprite streamer luminosity near the stratopause. *Geophysical Research Letters*, *46*, 12572–12579. https://doi.org/10.1029/2019GL084331

Gijben, M. (2012). The lightning climatology of South Africa. *South African Journal of Science*, *108*(3), 1–10. https://doi.org/10.4102/sajs.v108i3/4.740

Goodman, S. J., Christian, H. J., & Rust, W. D. (1988). A comparison of the optical pulse characteristics of intracloud and cloud-to-ground lightning as observed above clouds. *Journal of Applied Meteorology*, *27*(12), 1369–1381. https://doi.org/10.1175/1520-0450(1988)027⟨1369:ACOTOP⟩2.0.CO;2

Hersbach, H., Bell, B., Berrisford, P., Hirahara, S., Horányi, A., Muñoz-Sabater, J., et al. (2020). The ERA5 global reanalysis. *Quarterly Journal of the Royal Meteorological Society*, *146*(730), 1999–2049. https://doi.org/10.1002/qj.3803

Heymsfield, A. J., Schmitt, C., & Bansemer, A. (2013). Ice cloud particle size distributions and pressure-dependent terminal velocities from in situ observations at temperatures from 0°C to −86°C. *Journal of the Atmospheric Sciences*, *70*(12), 4123–4154. https://doi.org/10.1175/jas-d-12-0124.1

Homeyer, C. R., & Kumjian, M. R. (2015). Microphysical characteristics of overshooting convection from polarimetric radar observations. *Journal of the Atmospheric Sciences*, *72*(2), 870–891. https://doi.org/10.1175/jas-d-13-0388.1

Hou, W., Zhang, Q., Zhang, J., Wang, L., & Shen, Y. (2018). A new approximate method for lightning-radiated ELF/VLF ground wave propagation over intermediate ranges. *International Journal of Antennas and Propagation*, *2018*, 9353294. https://doi.org/10.1155/2018/9353294

Husbjerg, L. S., Neubert, T., Chanrion, O., Dimitriadou, K., Li, D., Stendel, M., et al. (2022). Observations of blue corona discharges in thunderclouds. *Geophysical Research Letters*, *49*, e2022GL099064. https://doi.org/10.1029/2022GL099064

Jacobson, A. R., & Light, T. E. L. (2012). Revisiting "Narrow Bipolar Event" intracloud lightning using the FORTE satellite. *Annales Geophysicae*, *30*(2), 389–404. https://doi.org/10.5194/angeo-30-389-2012

Jacobson, M. (2005). *Fundamentals of atmospheric modeling* (2nd ed.). Cambridge University Press. https://doi.org/10.1017/CBO9781139165389

Kašpar, P., Santolík, O., Kolmašová, I., & Farges, T. (2017). A model of preliminary breakdown pulse peak currents and their relation to the observed electric field pulses. *Geophysical Research Letters*, *44*, 596–603. https://doi.org/10.1002/2016GL071483

Knollenberg, R. G., Kelly, K., & Wilson, J. C. (1993). Measurements of high number densities of ice crystals in the tops of tropical cumulonimbus. *Journal of Geophysical Research*, *98*(D5), 8639–8664. https://doi.org/10.1029/92JD02525

Kolmašová, I., Santolík, O., Farges, T., Cummer, S. A., Lán, R., & Uhlíř, L. (2016). Subionospheric propagation and peak currents of preliminary breakdown pulses before negative cloud-to-ground lightning discharges. *Geophysical Research Letters*, *43*, 1382–1391. https://doi.org/10.1002/2015GL067364

Krämer, M., Rolf, C., Spelten, N., Afchine, A., Fahey, D., Jensen, E., et al. (2020). A microphysics guide to cirrus—Part 2: Climatologies of clouds and humidity from observations. *Atmospheric Chemistry and Physics*, *20*(21), 12569–12608. https://doi.org/10.5194/acp-20-12569-2020

Krapivsky, P. L., Redner, S., & Ben-Naim, E. (2010). *A kinetic view of statistical physics*. Cambridge University Press. https://doi.org/10.1017/CBO9780511780516

Kuo, C. L., Su, H. T., & Hsu, R. R. (2015). The blue luminous events observed by ISUAL payload on board FORMOSAT-2 satellite. *Journal of Geophysical Research: Space Physics*, *120*, 9795–9804. https://doi.org/10.1002/2015JA021386

Laby, T. H., Mcneill, J. J., Nicholls, F. G., & Nickson, A. F. B. (1940). Wave form, energy and reflexion by the ionosphere, of atmospherics. *Proceedings of the Royal Society A: Mathematical, Physical and Engineering Sciences*, *174*(957), 145–163. https://doi.org/10.1098/rspa.1940.0012

Li, D., Liu, F., Pérez-Invernón, F. J., Lu, G., Qin, Z., Zhu, B., & Luque, A. (2020). On the accuracy of ray-theory methods to determine the altitudes of intracloud electric discharges and ionospheric reflections: Application to narrow bipolar events. *Journal of Geophysical Research: Atmospheres*, *125*, e2019JD032099. https://doi.org/10.1029/2019JD032099

Li, D., Luque, A., Gordillo-Vázquez, F. J., Liu, F., Lu, G., Neubert, T., et al. (2021). Blue flashes as counterparts to narrow bipolar events: The optical signal of shallow in-cloud discharges. *Journal of Geophysical Research: Atmospheres*, *126*, e2021JD035013. https://doi.org/10.1029/2021JD035013

Liu, F., Lu, G., Neubert, T., Lei, J., Chanrion, O., Østgaard, N., et al. (2021). Optical emissions associated with narrow bipolar events from thunderstorm clouds penetrating into the stratosphere. *Nature Communications*, *12*, 6631. https://doi.org/10.1038/s41467-021-26914-4

Liu, F., Zhu, B., Lu, G., Lei, J., Shao, J., Chen, Y., et al. (2021). Meteorological and electrical conditions of two mid-latitude thunderstorms producing blue discharges. *Journal of Geophysical Research: Atmospheres*, *126*, e2020JD033648. https://doi.org/10.1029/2020JD033648

Liu, F., Zhu, B., Lu, G., Qin, Z., Lei, J., Peng, K.-M., et al. (2018). Observations of blue discharges associated with negative narrow bipolar events in active deep convection. *Geophysical Research Letters*, *45*, 2842–2851. https://doi.org/10.1002/2017GL076207

Liu, Z., Koh, K. L., Mezentsev, A., Enno, S. E., Sugier, J., & Fullekrug, M. (2018). Lightning sferics: Analysis of the instantaneous phase and frequency inferred from complex waveforms. *Radio Science*, *53*, 448–457. https://doi.org/10.1002/2017RS006451

Luque, A., Gordillo-Vázquez, F. J., Li, D., Malagón-Romero, A., Pérez-Invernón, F. J., Schmalzried, A., et al. (2020). Modeling lightning observations from space-based platforms (CloudScat.jl 1.0). *Geoscientific Model Development*, *13*(11), 5549–5566. https://doi.org/10.5194/gmd-13-5549-2020

Marchand, M., Hilburn, K., & Miller, S. D. (2019). Geostationary lightning mapper and Earth networks lightning detection over the contiguous United States and dependence on flash characteristics. *Journal of Geophysical Research: Atmospheres*, *124*, 11552–11567. https://doi.org/10.1029/2019JD031039

Montanyà, J., López, J. A., Morales Rodriguez, C. A., Van Der Velde, O. A., Fabró, F., Pineda, N., et al. (2021). A simultaneous observation of lightning by ASIM, Colombia-lightning mapping array, GLM, and ISS-LIS. *Journal of Geophysical Research: Atmospheres*, *126*, e2020JD033735. https://doi.org/10.1029/2020JD033735

Neubert, T., Chanrion, O., Heumesser, M., Dimitriadou, K., Husbjerg, L., Rasmussen, I. L., et al. (2021). Observation of the onset of a blue jet into the stratosphere. *Nature*, *589*(7842), 371–375. https://doi.org/10.1038/s41586-020-03122-6

Neubert, T., Østgaard, N., Reglero, V., Blanc, E., Chanrion, O., Oxborrow, C. A., et al. (2019). The ASIM mission on the International Space Station. *Space Science Reviews*, *215*(2), 26. https://doi.org/10.1007/s11214-019-0592-z

Neubert, T., Østgaard, N., Reglero, V., Chanrion, O., Heumesser, M., Dimitriadou, K., et al. (2020). A terrestrial gamma-ray flash and ionospheric ultraviolet emissions powered by lightning. *Science*, *367*(6474), 183–186. https://doi.org/10.1126/science.aax3872

Østgaard, N., Cummer, S. A., Mezentsev, A., Luque, A., Dwyer, J., Neubert, T., et al. (2021). Simultaneous observations of EIP, TGF, Elve, and optical lightning. *Journal of Geophysical Research: Atmospheres*, *126*, e2020JD033921. https://doi.org/10.1029/2020JD033921

Peterson, M. (2019). Using lightning flashes to image thunderclouds. *Journal of Geophysical Research: Atmospheres*, *124*, 10175–10185. https://doi.org/10.1029/2019JD031055

Peterson, M., Light, T. E. L., & Shao, X. (2021). Combined optical and radio-frequency measurements of a lightning megaflash by the FORTE satellite. *Journal of Geophysical Research: Atmospheres*, *126*, e2020JD034411. https://doi.org/10.1029/2020JD034411

Price, C., Greenberg, E., Yair, Y., Sátori, G., Bór, J., Fukunishi, H., & Sternlieb, A. (2004). Ground-based detection of TLE-producing intense lightning during the MEIDEX mission on board the space shuttle Columbia. *Geophysical Research Letters*, *31*, L20107. https://doi.org/10.1029/2004GL020711

Protat, A., Mcfarquhar, G. M., Um, J., & Delanoë, J. (2011). Obtaining best estimates for the microphysical and radiative properties of tropical ice clouds from TWP-ICE in situ microphysical observations. *Journal of Applied Meteorology and Climatology*, *50*(4), 895–915. https://doi.org/10.1175/2010jamc2401.1

Said, R. K., Inan, U. S., & Cummins, K. L. (2010). Long-range lightning geolocation using a VLF radio atmospheric waveform bank. *Journal of Geophysical Research*, *115*, D23108. https://doi.org/10.1029/2010JD013863

Said, R. K., & Murphy, M. (2016). GLD360 upgrade: Performance analysis and applications. In *24th International Lightning Detection Conference and Sixth International Lightning Meteorology Conference, American Institute of Physics Conference Series*.

Sato, M., Ushio, T., Morimoto, T., Kikuchi, M., Kikuchi, H., Adachi, T., et al. (2015). Overview and early results of the Global Lightning and Sprite Measurements mission. *Journal of Geophysical Research: Atmospheres*, *120*, 3822–3851. https://doi.org/10.1002/2014JD022428

Schmitt, C. G., & Heymsfield, A. J. (2009). The size distribution and mass-weighted terminal velocity of low-latitude tropopause cirrus crystal populations. *Journal of the Atmospheric Sciences*, *66*(7), 2013–2028. https://doi.org/10.1175/2009jas3004.1

Schonland, B. F. J., Elder, J. S., Hodges, D. B., Phillips, W. E., & Van Wyk, J. W. (1940). The wave form of atmospherics at night. *Proceedings of the Royal Society A: Mathematical, Physical and Engineering Sciences*, *176*(965), 180–202. https://doi.org/10.1098/rspa.1940.0085

Shao, X., & Jacobson, A. R. (2009). Model simulation of very low-frequency and low-frequency lightning signal propagation over intermediate ranges. *IEEE Transactions on Electromagnetic Compatibility.*, *51*(3), 519–525. https://doi.org/10.1109/TEMC.2009.2022171

Smith, D. A., Heavner, M. J., Jacobson, A. R., Shao, X. M., Massey, R. S., Sheldon, R. J., & Wiens, K. C. (2004). A method for determining intracloud lightning and ionospheric heights from VLF/LF electric field records. *Radio Science*, *39*, RS1010. https://doi.org/10.1029/2002RS002790

Soler, S., Pérez-Invernón, F. J., Gordillo-Vázquez, F. J., Luque, A., Li, D., Malagón-Romero, A., et al. (2020). Blue optical observations of narrow bipolar events by ASIM suggest corona streamer activity in thunderstorms. *Journal of Geophysical Research: Atmospheres*, *125*, e2020JD032708. https://doi.org/10.1029/2020JD032708

Taylor, S., Stier, P., White, B., Finkensieper, S., & Stengel, M. (2017). Evaluating the diurnal cycle in cloud top temperature from SEVIRI. *Atmospheric Chemistry and Physics*, *17*(11), 7035–7053. https://doi.org/10.5194/acp-17-7035-2017

Thomson, L. W., & Krider, E. P. (1982). The effects of clouds on the light produced by lightning. *Journal of the Atmospheric Sciences*, *39*(9), 2051–2065. https://doi.org/10.1175/1520-0469(1982)039⟨2051:TEOCOT⟩2.0.CO;2

van der Velde, O. A., Montanyà, J., Neubert, T., Chanrion, O., Østgaard, N., Goodman, S., et al. (2020). Comparison of high-speed optical observations of a lightning flash from space and the ground. *Earth and Space Science*, *7*, e2020EA001249. https://doi.org/10.1029/2020EA001249

Vaughan, M. A., Young, S. A., Winker, D. M., Powell, K. A., Omar, A. H., Liu, Z., et al. (2004). Fully automated analysis of space-based lidar data: An overview of the CALIPSO retrieval algorithms and data products. *Proceedings of SPIE*, *5*(575), 16–30. https://doi.org/10.1117/12.572024

Vaughan, O. H., Blakeslee, R., Boeck, W. L., Vonnegut, B., Brook, M., & McKune, J. J. (1992). A cloud-to-space lightning as recorded by the space shuttle payload-bay TV cameras. *Monthly Weather Review*, *120*(7), 1459–1461. https://doi.org/10.1175/1520-0493(1992)120⟨1459:ACTSLA⟩2.0.CO;2

Williams, E. R., Geotis, S. G., Renno, N., Rutledge, S. A., Rasmussen, E., & Rickenbach, T. (1992). A radar and electrical study of tropical "hot towers". *Journal of the Atmospheric Sciences*, *49*(15), 1386–1395. https://doi.org/10.1175/1520-0469(1992)049⟨1386:ARAESO⟩2.0.CO;2

Winker, D. M., Pelon, J. R., & McCormick, M. P. (2003). The CALIPSO mission: Spaceborne lidar for observation of aerosols and clouds. *Proceedings of SPIE*, *4*(893), 1–11. https://doi.org/10.1117/12.466539

Yair, Y., Price, C., Levin, Z., Joseph, J., Israelevitch, P., Devir, A., et al. (2003). Sprite observations from the space shuttle during the Mediterranean Israeli dust experiment (MEIDEX). *Journal of Atmospheric and Solar-Terrestrial Physics*, *65*(5), 635–642. https://doi.org/10.1016/S1364-6826(02)00332-2

Yair, Y., Price, C., Ziv, B., Israelevich, P. L., Sentman, D. D., São-Sabbas, F. T., & Yaron, O. (2005). Space shuttle observation of an unusual transient atmospheric emission. *Geophysical Research Letters*, *32*, L02801. https://doi.org/10.1029/2004GL021551

Yair, Y., Rubanenko, L., Mezuman, K., Elhalel, G., Pariente, M., Glickman-Pariente, M., et al. (2013). New color images of transient luminous events from dedicated observations on the International Space Station. *Journal of Atmospheric and Solar-Terrestrial Physics*, *102*, 140–147. https://doi.org/10.1016/j.jastp.2013.05.004

Zhang, D., & Cummins, K. L. (2020). Time evolution of satellite-based optical properties in lightning flashes, and its impact on GLM flash detection. *Journal of Geophysical Research: Atmospheres*, *125*, e2019JD032024. https://doi.org/10.1029/2019JD032024

Zhou, X., Wang, J., Ma, Q., Huang, Q., & Xiao, F. (2021). A method for determining D region ionosphere reflection height from lightning skywaves. *Journal of Atmospheric and Solar-Terrestrial Physics*, *221*, 105692. https://doi.org/10.1016/j.jastp.2021.105692

Zhu, Y., Stock, M., Lapierre, J., & DiGangi, E. (2022). Upgrades of the Earth Networks Total Lightning Network in 2021. *Remote Sensing*, *14*(9), 2209. https://doi.org/10.3390/rs14092209